Effect of solutal Marangoni convection on motion, coarsening, and coalescence of droplets in a monotectic system

F. Wang,[1,2,*] A. Choudhury,[2] M. Selzer,[1,2] R. Mukherjee,[1,2] and B. Nestler[1,2,†]

[1]*Institute of Materials and Processes, Karlsruhe University of Applied Sciences, Moltkestrasse 30, 76133, Karlsruhe, Germany*

[2]*Institute of Applied Materials, Karlsruhe Institute of Technology, Haid-und-Neu Strasse 7, 76131 Karlsruhe, Germany*

(Received 24 August 2012; published 20 December 2012)

In this paper, we study the effect of solutal Marangoni convection (SMC) on the microstructure evolution in a monotectic system, using the convective Cahn-Hilliard and Navier-Stokes equations with a capillary tensor contributed by the chemical concentration gradient. At first, we simulate the spontaneous motion of two distant droplets induced by SMC and compare our results with an analytical solution. We then compute the coalescence of two droplets in contact and coarsening of two distant droplets considering different sizes. We further study the influence of SMC on the evolution of phase separation processes inside the spinodal region for Fe-50 at %Sn and Fe-40 at %Sn alloys. In the former case, we rationalize our results using Fourier spectra and in the latter case, we compare the size distribution of droplets with the LSW theory.

DOI: 10.1103/PhysRevE.86.066318 PACS number(s): 47.55.nb, 64.75.Op, 64.70.pm, 64.75.Cd

I. INTRODUCTION

Marangoni convection, either induced by thermal gradients or arising from concentration gradients, plays an important role in monotectic systems [1–4] and other materials [5,6] and has been investigated, both through experiments [6–8] and simulations [1,3,4,9,12,28]. We focus here on the Marangoni convection induced by the chemical concentration gradients under isothermal condition in a monotectic system, also known as solutal Marangoni convection (SMC) or Gibbs-Marangoni effect. Due to a region of miscibility gap in the phase diagram of monotectics, the primary liquid is unstable and decomposes into two liquids, indicated by l_1 and l_2, respectively, inside the spinodal region [13]. The Marangoni convection in the consequent mass transfer between these two liquids are of significant importance [9,15–18].

In this work, by utilizing a higher-order polynomial to describe the free energy of the liquid and applying the convective Cahn-Hilliard and Navier-Stokes equations with a capillary tensor contributed by the concentration gradient, we simulate the spontaneous motion of two distant droplets induced by SMC and compare it with analytical solutions. When the distance between two droplets is less than twice of the interface width, we compute the coalescence process assisted by SMC. Additionally, the coarsening process of two distant droplets with different sizes affected by SMC is investigated. Furthermore, we study the phase separation processes in Fe-50 at %Sn and Fe-40 at %Sn alloys with and without SMC. For a different second-phase volume fraction, bicontinuous phase separation morphologies are obtained in Fe-50 at %Sn alloy, in contrast to droplet morphologies being achieved in Fe-40 at %Sn alloy. The influence of SMC on the evolution modes during the phase separation process in Fe-50 at %Sn alloy is analyzed and the size distributions of droplets in the Fe-40 at %Sn alloy with and without SMC are studied, in comparison with the LSW theory.

The scheme of this paper is as follows. Sections II A and II B depict the equations for concentration evolution and for Marangoni convection, respectively. Sections II C and II D describe the nondimensionalization procedure for the simulation parameters and stability condition for the governing equations, respectively. At the final part of Sec. II, we derive the surface energy and interface width. Section III A deals with the spontaneous motion of two distant droplets induced by SMC analytically, and Sec. III B presents the simulation results. Consequently, we compute the coarsening and coalescence of two droplets under the influence of SMC in Sec. IV B. Sections V A and V B comprise the phase separation including SMC in Fe-50 at %Sn and Fe-40 at %Sn alloys, respectively. Finally, we conclude the paper in Sec. VI.

II. MODEL DESCRIPTION

A. Concentration equation

For a binary alloy with components A and B, we follow Ref. [19] and formulate a free energy functional, depending on concentration c and temperature T, as

$$\mathcal{F}(c,T) = \int_V [f(c,T) + \varepsilon_c a_c(c,\nabla c)]dV,$$

where V is the region occupied by the system, and $f(c,T)$ is the bulk free energy density of the phases, ε_c is a small-length scale parameter related to the interface thickness. The concentration c differentiates between the liquid phases.

The gradient term for the concentration field can be written as

$$a_c(c,\nabla c) = \gamma_c|\nabla c|^2,$$

with γ_c being a parameter related to the surface energy density.

Based on a regular solution model, the free energy density $f(c,T)$ is written as

$$f(c,T) = \frac{RT}{v_m}[c\ln c + (1-c)\ln(1-c)] + \sum_{j=1}^{2}\Omega_j c^j(1-c)^j. \quad (1)$$

*fei.wang@hs-karlsruhe.de

†britta.nestler@kit.edu

TABLE I. Parameters for simulation.

Parameters		Value
$\tilde{\varepsilon}_c$	Parameter related to interface width	2
$\tilde{\gamma}_c$	Surface energy density	1
$\Delta x = \Delta y$	Discretization space step	1
Δt	Discretization time step	Eq. (8)
M	Marangoni number	$10 \sim 1000$
Re	Reynolds number	0.01
$\Omega_1/(RT_m/v_m)$	Interaction coefficient	0.345
$\Omega_2/(RT_m/v_m)$	Interaction coefficient	4.379
L	Simulation domain size	300×300
$d_0(nm)$	Capillary length	0.01
$\eta(Pas)$	Dynamic viscosity	1×10^{-3}
$\rho(kg/m^3)$	Density	1×10^{4}
$D_l(m^2/s)$	Diffusion coefficient	1×10^{-9}
β	Safety parameter	0.2
$RT_m/v_m(J/m^3)$	Scaling factor of free energy	1×10^{9}

Here, R is the ideal gas constant, v_m denotes the molar volume assumed to be constant. T and c are the temperature and the concentration, respectively. Ω_j are constants listed in Table I. The free energy density is plotted with respect to concentration and temperature in Fig. 1(a), based on which, the miscibility gap and the spinodal line are shown in Fig. 1(b).

The mass conservation of the system requires

$$\frac{\partial c}{\partial t} + \mathbf{u}\cdot\nabla c = -\nabla\cdot(\mathbf{J}+\zeta),$$

where $\mathbf{u}$ is the velocity of convection, ζ is the fluctuation, and $\mathbf{J}$ is the mass flux because of diffusion, which may be expressed as

$$\mathbf{J} = -\Lambda(c)\nabla\mu, \tag{2}$$

where μ is the chemical potential expressed as

$$\mu = \frac{\delta F}{\delta c} = \frac{\partial f(c,T)}{\partial c} - 2\varepsilon_c\gamma_c\nabla^2 c.$$

The mobility in Eq. (2) reads

$$\Lambda(c) = \frac{v_m}{RT} D_l c(1-c),$$

where D_l is the diffusion coefficient in liquid.

B. Solutal Marangoni convection

We use a Lagrangian formalism to introduce the contribution of the concentration field in the Navier-Stokes equation. From the Lagrangian energy density being written as

$$\mathcal{L} = f(c,T) + \varepsilon_c\gamma_c(\nabla c)^2,$$

a relation can be derived as (derivation is elaborated in Appendix A; more detail work can be found in Ref. [20])

$$\frac{\partial}{\partial x_i}\left[\frac{\partial\mathcal{L}}{\partial(\partial_i c)}\frac{\partial c}{\partial x_j} - \mathcal{L}\delta_{ij}\right] = 0.$$

From the above equation and as discussed in Refs. [3,21,22], the stress tensor appears to be

$$\mathbf{\Theta} = 2\varepsilon_c\gamma_c\nabla c\otimes\nabla c - \mathcal{L}\mathbf{I}, \tag{3}$$

which appears in components as

$$\mathbf{\Theta}_{ij} = 2\varepsilon_c\gamma_c\frac{\partial c}{\partial x_i}\frac{\partial c}{\partial x_j} - \mathcal{L}\delta_{ij}.$$

The stress tensor satisfies the conservation law

$$\nabla\cdot\mathbf{\Theta} = 0.$$

The contribution of capillary forces in this equation is given by the conservative term $-\nabla\cdot\mathbf{\Theta}$, which, included in the generalized Navier-Stokes equation, reads as

$$\rho\left(\frac{\partial\mathbf{u}}{\partial t} + \mathbf{u}\cdot\nabla\mathbf{u}\right) = -\nabla p + \nabla\cdot[(\varepsilon_c\gamma_c\nabla c\cdot\nabla c + f)\mathbf{I} - 2\varepsilon_c\gamma_c\nabla c\otimes\nabla c] + \eta\nabla\cdot(\nabla\mathbf{u}). \tag{4}$$

Here, ρ is the density, p is the pressure, $\mathbf{I}$ is the unit tensor, and η is the dynamic viscosity.

The similar formulation of the convective Cahn-Hilliard equation can be found in Refs. [10,11].

C. Nondimensionalization and parameters

By choosing $r = d_0\tilde{r}$, $f = \frac{RT}{v_m}\tilde{f}$, $\gamma_c = \frac{RT}{v_m}d_0\tilde{\gamma}_c$, $t = \frac{d_0^2}{D_l}\tau$, $\varepsilon_c = d_0\tilde{\varepsilon}_c$, $\mathbf{u} = \frac{D_l}{d_0}\tilde{\mathbf{u}} = u^*\tilde{\mathbf{u}}$, and $p = \rho u^{*2}\tilde{p}$, the dimensionless concentration equation is rearranged to

$$\frac{\partial c}{\partial\tau} + \tilde{u}\cdot\tilde{\nabla}c = \tilde{\nabla}\cdot\left[c(1-c)\tilde{\nabla}\left(\frac{\partial\tilde{f}}{\partial c} - 2\tilde{\varepsilon}_c\tilde{\gamma}_c\tilde{\nabla}^2 c\right) + \zeta\right], \tag{5}$$

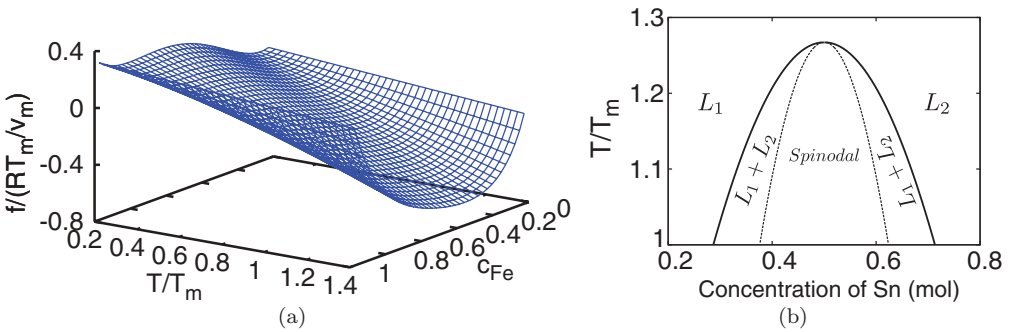

FIG. 1. (Color online) (a) The free energy of the liquid as a function of concentration and temperature, (b) the miscibility gap and spinodal region plotted according to the free energy given by Eq. (1).

and the Navier-Stokes equation derives as

$$\frac{\partial \tilde{\mathbf{u}}}{\partial \tau} + \tilde{\mathbf{u}} \cdot \tilde{\nabla}\tilde{\mathbf{u}} = -\tilde{\nabla}\tilde{p} + M\tilde{\nabla} \cdot [(\tilde{\varepsilon}_c \tilde{\gamma}_c \tilde{\nabla} c \cdot \tilde{\nabla} c + \tilde{f})\mathbf{I} - 2\tilde{\varepsilon}_c \tilde{\gamma}_c \tilde{\nabla} c \otimes \tilde{\nabla} c] + \frac{1}{\mathrm{Re}} \tilde{\nabla} \cdot (\tilde{\nabla}\tilde{\mathbf{u}}), \quad (6)$$

where M and Re are Marangoni and Reynolds numbers, expressed as $RTd_0^2/(\rho D_l^2 v_m)$ and $\rho u^* d_0/\eta$, respectively.

In addition, because our system is assumed to be an incompressible system and the density of two liquids is presumed to be identical, we get the equation

$$\nabla \cdot \tilde{\mathbf{u}} = 0. \quad (7)$$

The simulation parameters refer to Fe-Sn system and are tabulated in Table I.

D. Stability

The stability condition for the Navier-Stokes equation can be chosen as [24]

$$\Delta t < \beta \min \left\{ \frac{1}{2}\mathrm{Re}\left(\frac{1}{\Delta x^2} + \frac{1}{\Delta y^2}\right)^{-1}, \frac{\Delta x}{|u_{\max}|}, \frac{\Delta y}{|v_{\max}|} \right\}. \quad (8)$$

Here, β is a safety parameter, Re is the Reynolds number, and $|u_{\max}|$ and $|v_{\max}|$ are the maximal velocity in the x and the y directions, respectively.

E. Relation to sharp-interface limit

In this section, we derive the surface energy and interface width for a planar interface. The surface energy can be written as the total grand chemical potential excess at the interface. This is elaborated as

$$\sigma = \int_X \left\{ [f(c,T) - \mu_{\mathrm{eq}} c] - (f_{\mathrm{eq}} - \mu_{\mathrm{eq}} c_{\mathrm{eq}}) + \varepsilon_c \gamma_c \left(\frac{\partial c}{\partial x}\right)^2 \right\} dx. \quad (9)$$

The equilibrium equation is obtained by setting $\frac{\partial c}{\partial t} = 0$, which results in

$$\mu_{\mathrm{eq}} = \frac{\partial f_{\mathrm{eq}}}{\partial c} - 2\varepsilon_c \gamma_c \frac{\partial^2 c}{\partial x^2}. \quad (10)$$

Multiplying both sides with $\frac{\partial c}{\partial x}$ and integrating from $-\infty$ to x yields

$$[f(c,T) - \mu_{\mathrm{eq}} c] - (f_{\mathrm{eq}} - \mu_{\mathrm{eq}} c_{\mathrm{eq}}) = \varepsilon_c \gamma_c \left(\frac{\partial c}{\partial x}\right)^2.$$

Because the free energy of the liquid is almost symmetric with respect to 0.5 of the molar concentration of Fe, it is reasonable to assume $\mu_{\mathrm{eq}} \approx 0$ in Eq. (10); thus, combining with Eq. (9), we get the surface energy as

$$\sigma = 2\varepsilon_c \gamma_c \int_X \left(\frac{\partial c}{\partial x}\right)^2 dx.$$

Moreover, the interface width λ can be calculated by the following equation,

$$\lambda = \int dx = \sqrt{\gamma_c \varepsilon_c} \int_{c_1}^{c_2} \frac{1}{\sqrt{f(c,T) - f_{\mathrm{eq}}}} dc. \quad (11)$$

III. THE MOTION OF DROPLETS INDUCED BY SMC

If two equal-sized droplets of l_2 phase are placed in close proximity inside l_1 matrix, they will be in equilibrium, because they have the same curvature. However, if there is a weak solute transport between the droplets of l_2 and the continuous phase l_1, the stationary state will be broken due to the convection, which results from the nonuniform concentration gradient along the surface of the droplets [16].

Hereafter, we first analytically derive the velocity of motion of the barycenter of each droplet induced by SMC, and then we compare it with the simulation results, which is performed by solving Eqs. (5) and (6).

A. Analytical solution

In order to get the analytical solution, we choose a bipolar coordinate system, which is associated with the cylindrical system by the following relations,

$$z = \frac{\chi \sin h\iota}{\cosh \iota - \cos \varphi}, \quad x = \frac{\chi \sin \varphi}{\cosh \iota - \cos \varphi},$$

where z and x are the coordinates in the cylindrical system, ι and φ are the coordinates in the bipolar system. $\chi = \sinh \mathrm{a}$, with a being the radius of the droplet in the bipolar coordinate system, as schematically illustrated in Fig. 2. It can be related to the separation distance between two droplets as

$$a = \left| \cosh^{-1}\left(\tfrac{1}{2}d + 1\right) \right|.$$

It is worthy to point out that we use (a) and $(-a)$ to denote the two droplets, and (0) represents the continuous phase, in the following derivation.

When the Péclet number fulfills $\frac{RV}{D} \ll 1$, the concentration equation becomes a Laplace equation

$$\nabla^2 c = 0.$$

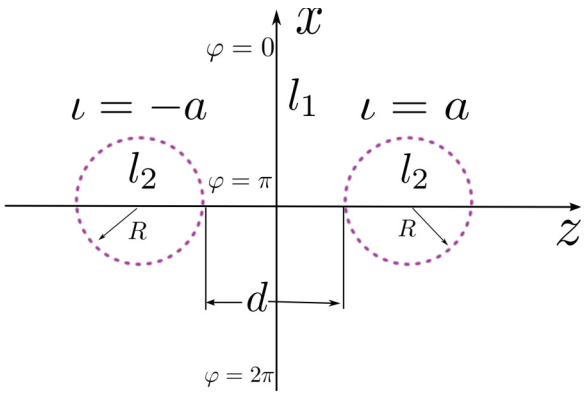

FIG. 2. (Color online) Schematic figure referred to in Ref. [25].

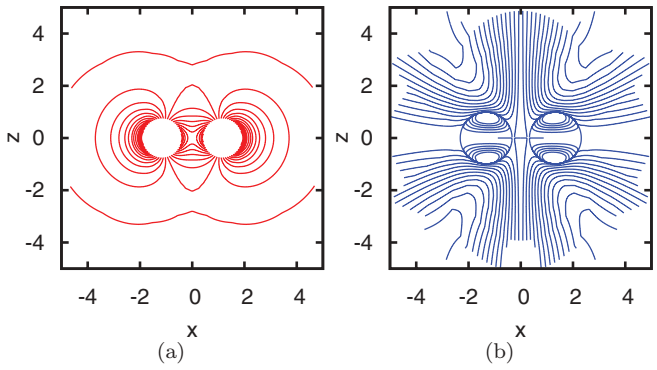

FIG. 3. (Color online) Isoconcentration (left) and stream line (right) from analytical solution under the condition: $\varsigma = 2$, $d/R = 0.67$.

Following Ref. [16,25], its general solution can be expressed as

$$c = \sqrt{(\cosh\iota - \cos\varphi)} \sum_{n=1}^{n=\infty} G_n \cosh\left[\left(n + \frac{1}{2}\right)\iota\right] P_n(\cos\varphi). \tag{12}$$

Here, $P_n(\cos\varphi)$ are Legendre polynomials, G_n are coefficients determined below.

We employ the following boundary condition for mass transfer between the dispersed and continuous phase [26],

$$\frac{\cosh\iota - \cos\varphi}{\chi}\frac{\partial c}{\partial \iota} = \varsigma(1-c), \quad \iota = a,$$
$$\frac{\cosh\iota - \cos\varphi}{\chi}\frac{\partial c}{\partial \iota} = \varsigma(c-1), \quad \iota = -a,$$

where ς is the Sherwood number, which denotes the ratio of convective to diffusive mass transport. The above equations result in the following equations for the coefficients G_n:

$$g_{-1}^n G_{n-1} - g_0^n G_n + g_1^n G_{n+1} = -2\sqrt{2}\chi\varsigma e^{-(n+\frac{1}{2})a}, \tag{13}$$

where the coefficients g_{-1}^n, g_0^n, and g_1^n are given in Appendix B. With the methods suggested in Refs. [16,25], we can obtain the coefficients G_n. Substituting these into Eq. (12), the concentration can be achieved and the isoconcentration lines are plotted in Fig. 3(a) with $d/R = 0.67$ (R is the radius of droplets) and $\varsigma = 2$.

The velocity can be related to the Stokes stream function as

$$u_\iota = \frac{(\cosh\iota - \cos\varphi)^2}{\sin h^2 a \sin h\varphi}\frac{\partial\psi}{\partial\varphi},$$
$$u_\varphi = -\frac{(\cosh\iota - \cos\varphi)^2}{\sin h^2 a \sin h\varphi}\frac{\partial\psi}{\partial\iota}, \tag{14}$$

in which the Stokes stream function satisfies the following equation:

$$\Phi^2(\Phi^2\psi) = 0, \tag{15}$$

with Φ^2 being expressed as

$$\Phi^2 = (\cosh\iota - \cos\varphi)\left\{\frac{\partial}{\partial\iota}\left[(\cosh\iota - \cos\varphi)\frac{\partial}{\partial\iota}\right] + (1-\cos^2\varphi)\frac{\partial}{\partial\cos\varphi}\left[(\cosh\iota - \cos\varphi)\frac{\partial}{\partial\cos\varphi}\right]\right\}.$$

The solution of Eq. (15) is first proposed by Ref. [27] as

$$\psi(\iota,\varphi) = (\cosh\iota - \cos\varphi)^{-\frac{3}{2}} \sum_{n=1}^{\infty} X_n^{(i)} C_{n+1}^{-\frac{1}{2}}(\cos\varphi),$$
$$i = a, -a, 0,$$

with

$$X_n^{(0)} = I_n^{(0)}\cosh\left[\left(n-\tfrac{1}{2}\right)\iota\right] + J_n^{(0)}\sin h\left[\left(n-\tfrac{1}{2}\right)\iota\right] + K_n^{(0)}\cosh\left[\left(n+\tfrac{3}{2}\right)\iota\right] + L_n^{(0)}\sin h\left[\left(n+\tfrac{3}{2}\right)\iota\right],$$
$$X_n^{(a)} = I_n^{(a)} e^{-(n-\frac{1}{2})\iota} + K_n^{(a)} e^{-(n+\frac{3}{2})\iota},$$
$$X_n^{(-a)} = I_n^{(a)} e^{(n-\frac{1}{2})\iota} + K_n^{(a)} e^{(n+\frac{3}{2})\iota}.$$

The coefficients $I_n^{(0)}$,$J_n^{(0)}$, $K_n^{(0)}$,$L_n^{(0)}$,$I_n^{(a)}$,$K_n^{(a)}$, $I_n^{(-a)}$, and $K_n^{(-a)}$ are determined by the boundary conditions following

$$\mathbf{u}^{(0)}\cdot\mathbf{n} = \mathbf{U}^{(a)}\cdot\mathbf{n}, \quad \iota = \pm a,$$
$$\tau_{\iota\varphi}^{(0)} - \tau_{\iota\varphi}^{(a)} = \pm\frac{\cosh\iota - \cos\varphi}{\sin ha}\frac{\partial c}{\partial\varphi}, \quad \iota = \pm a, \tag{16}$$

where $\tau_{\iota\varphi}$ is the tangential component of the viscous stress tensor, $\mathbf{n}$ is the unit normal to the surface of droplets in bipolar coordinates, $\mathbf{U}^{(a)}$ is the motion velocity of droplets, scaled by $(c_{l_1} - c_{l_2})\frac{\partial\sigma}{\partial c}/\eta$ and expressed as $\mathbf{U}^{(a)} = U\mathbf{i}_z$, where $\mathbf{i}_z$ is the unit vector along z axis.

Equation (16) generates a relation between U and the stream function as (see Appendix C)

$$\psi|_{l=\pm a} = -\frac{1}{2}U\frac{\chi^2\sin^2\varphi}{(\cosh\iota - \cos\varphi)^2}. \tag{17}$$

Substituting the expression of ψ and c into boundary conditions results in the following equation:

$$\Xi_n\mathbf{b}_n = \chi^2(\varsigma\chi\mathbf{t}_n - U\mathbf{v}_n), \tag{18}$$

where $\mathbf{b}_n = [I_n^{(0)}, J_n^{(0)}, K_n^{(0)}, L_n^{(0)}, I_n^{(a)}, K_n^{(a)}, I_n^{(-a)}, K_n^{(-a)}]^T$. Ξ_n, $\mathbf{t}_n$, and $\mathbf{v}_n$ are matrices with components related to n and G_n, given in Appendix B.

Assuming quasistationary state and requiring the force on each droplet to be zero, as proposed in Refs. [16,25], we obtain

$$\sum_{n=1}^{\infty}\left[I_n^{(0)} + K_n^{(0)}\right] = 0. \tag{19}$$

Combining Eqs. (8) and (9), we can get the motion velocity as a function of separation distance. Utilizing the velocity, we achieve the coefficients, $I_n^{(0)}$,$J_n^{(0)}$, $K_n^{(0)}$,$L_n^{(0)}$,$I_n^{(a)}$,$K_n^{(a)}$, $I_n^{(-a)}$, and $K_n^{(-a)}$ to obtain the Stokes stream function, as illustrated in Fig. 3(b).

B. Simulation results

As described at the beginning of this section, we place two equal-sized droplets (radius of 30 grid points) of l_2 phase with a distance above 20 grid cells apart, which is greater than double the interface width. It ensures that no coalescence and coarsening happen between them. The size of the simulation domain is 300 × 300 grid cells. Periodic boundary conditions are implemented for concentration and velocity field.

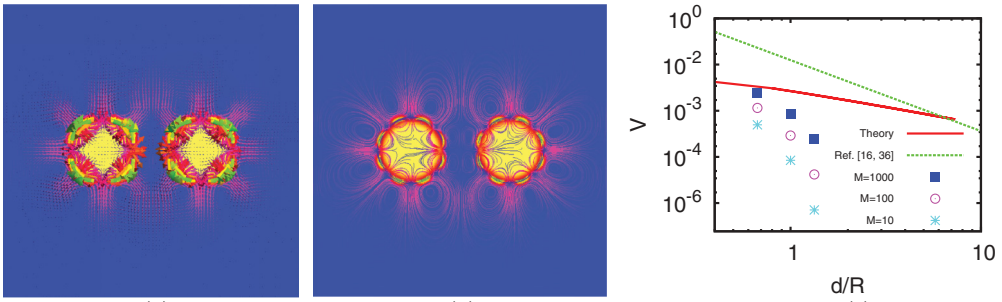

FIG. 4. (Color online) (a) The convection profile of SMC under the condition: $d = 40$, $R = 30$, $\varsigma = 2$, at simulation time of 2×10^5; (b) the stream line of SMC corresponding to image (a); (c) the motion velocity of the droplet's barycenter, varying with distance between droplets: the solid red line is the analytical results from Sec. III A, the dashed green line shows the result from Refs. [16,36], according to Eq. (18), and the star, circle, square symbols denote the simulation results at different Marangoni numbers.

Due to the application of solving equations based on an explicit finite difference discretization on a rectangular mesh, there are curvature differences along the surface of droplets after the filling of droplets into the simulation domain. We, therefore, use the following equation to smoothen the interface of each droplet before starting the simulation,

$$c_n = c_o + D_c \nabla^2 c_o,$$

where c_n and c_o are the new and old concentration, respectively, D_c is a coefficient set to be 0.05. After 20 steps of smoothening, the relative curvature differences (grid effect) along the droplets become less than 1% of the curvature of an ideal circle, such that the curvature differences due to filling can be neglected.

After the above precondition, we start simulations with a temperature being 5 K below the monotectic temperature, to make sure that the droplets maintain their size. However, due to this setting, the droplets grow a little in size and after a transient state reach the equilibrium with the matrix. After reaching equilibrium, these two droplets move toward each other due to SMC induced by the nonuniform concentration distribution along the surface of the droplets.

The convection pattern and stream line of convection for two droplets 40 grid cells apart, are shown in Figs. 4(a) and 4(b), respectively. Interestingly, several swirls appear around the interface of each droplet. This, in fact, is caused by introducing the term $\varepsilon_c \gamma_c (\nabla c \cdot \nabla c \mathbf{I} - 2 \nabla \otimes \nabla c)$ to calculate the convection, which results from the nonuniform concentration distribution along the surface of droplets. As we can see from the convection direction and the stream line, the swirls between the interdroplet region influences the motion of the droplets toward each other, whereas the swirls on the opposite sides of the droplets are likely to play a negative role.

The mass transfer along the surface of each droplet and between the two droplets are influenced by the convection through the convective term in the concentration equation, causing the shift in barycenter of each droplet. The velocity as a function of initial distance between the two droplets is shown in Fig. 4(c). The star, circle, and square symbols denote the simulated velocities when the Marangoni number is 10, 100, and 1000, respectively. The solid red line is the analytical result from Sec. III A and the dashed green line shows the result from Refs. [16,36], according to the equation

$$V = \frac{\varsigma}{2.5(\varsigma + 1)(\varsigma + 2)} \left(\frac{d}{R} \right)^{-2}. \tag{20}$$

As denoted by symbols representing the simulation results, the effect of convection is reduced with increasing the distance between the two droplets and becomes stronger while increasing the Marangoni number. The former tendency is easy to understand: The droplets with a larger distance have a comparable effect of convection at inner- and outer-droplet region and smaller concentration difference along the surface. While decreasing the distance between the droplets, the effect of inner swirls becomes stronger than outer swirls, and this, subsequently, causes a dramatic enhancement of the velocity. For comprehending the latter phenomenon, we can rewrite the Marangoni number as $M = (RT/v_m) d_0^2/(\rho D_l^2)$, where RT/v_m is a scaling factor derived from surface tension and capillary length. The increase of the Marangoni number from 10 to 100 or 1000 can be achieved by decreasing the diffusion coefficient to $D_l/\sqrt{10}$ or one order lower, which is possible in real alloys [23]. The trending of velocity versus initial distance between droplets, obtained from simulation, is quite similar to the one from Eq. (19), which is used to predict the case when $d \to \infty$.

However, the velocity obtained from our simulation using the stress tensor of Eq. (3) is less than that obtained from the analytical result. This may be due to the competition between the interdroplets swirls and the ones at the opposite sides of the droplets, which have not been considered in the analytical model. Decreasing the distance of the two droplets can strengthen the effect of convection, but due to the fact that we have a finite interface width, which has not been considered in the analytical model, the droplets are expected to undergo a coalescence process with the decrease in distance.

IV. COARSENING AND COALESCENCE INFLUENCED BY SMC

A. Transition from motion to coalescence

As described in Sec. III B, the two distant droplets move toward each other due to the SMC induced by the nonuniform concentration distribution along the surface. However, the interfaces of the two droplets can overlap each other after some

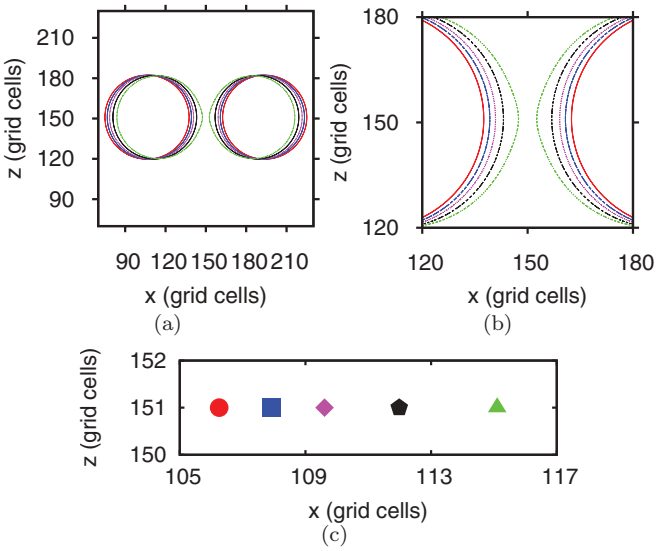

FIG. 5. (Color online) Transition from motion to coalescence: (a) the trace of the line with value of 0.5, of each droplet, when the initial distance between the two droplets is 30 grid cells and $M = 1000$. The solid red, dashed blue, dotted pink, dot dashed black, and dot dot dashed green lines correspond to the simulation time of 8 760, 27 760, 41 760, 52 760, and 55 160, respectively. (b) A zoom of panel (a). (c) The barycenter of the left droplet at the simulation time of 8 760, 27 760, 41 760, 52 760, and 55 160, represented by the red circle, blue square, pink lozenge, black pentagon, and green triangle, respectively.

time; thereafter, coalescence will be the dominant mechanism between them.

As illustrated in Fig. 5(a), we show the trace of the line with a value of 0.5, of each droplet, when the initial distance between the two droplets is 30 grid cells. The region between the two droplets is zoomed in Fig. 5(b). The solid red, dashed blue, dotted pink, dot dashed black, and dot dot dashed green lines correspond to the simulation time of 8 760, 27 760, 41 760, 52 760, and 55 160, respectively. From the figure we can see the droplets almost maintain the morphology till the time 52 760 during this process. However, the droplets develop protrusions in the x direction [see Fig. 5(b)], decreasing the distance between the droplets, which means that they go inside the coalescing stage.

In addition, Fig. 5(c) shows the barycenter of the left droplet at the simulation time of 8 760, 27 760, 41 760, 52 760, and 55 160, represented by the red circle, blue square, pink lozenge, black pentagon, and green triangle, respectively.

B. Coalescence

In this section, we investigate the effect of SMC on coalescence process. Initially, we put two droplets of l_2 phase in contact and inside the l_1 matrix, with a distance being less than double the interface width, as illustrated in Fig. 6(a). The concentration of Fe in the droplets and in the matrix are 0.92 and 0.7132, respectively.

With time, the two droplets join to reduce the total surface area, causing a concave region where two droplets contact each other. This, subsequently, induces a convection along the surface of each droplet due to the difference in concentration gradient.

We show the coalescing morphology at the initial stage in Fig. 6(a). The path of convection and stream line at the time of 3 220 while $M = 10$ are given in Figs. 6(b) and 6(c), respectively. The isolines for pressure caused by SMC corresponding to the state in Fig. 6(b) are plotted in Fig. 6(d). We take the following route to obtain the pressure profile. We first solve the Navier-Stokes equation with capillary tensor and then substitute the results into the Eq. (7) because of the assumption of incompressible flow, which results in a Poisson equation for the pressure. By employing SOR iteration to solve the Poisson equation, we thus obtain the pressure profile, which results from convection. For a detailed mathematical procedure, one may refer to Ref. [24].

To compare the coalescing process in the presence and absence of SMC, we calculate the height of neck as a function of time, as illustrated in Fig. 6(e). We include a schematic figure inside for better understanding of where we exactly measure the height of the neck. The dashed red, dot dashed green, and dot dot dashed pink lines represent the cases with SMC when $M = 10$, 100, and 1000, respectively. The solid blue line depicts the process only governed by diffusion. As we can see, the interfaces of the two droplets contact each other earlier and the height of the neck evolves faster while considering SMC. Moreover, the increase in Marangoni number from 10 to 1000 substantially raises the rate of coalescence.

C. Coarsening

Two droplets with different sizes and at a distance larger than double the interface width undergo an Oswald ripening process due to the Gibbs-Thomson effect. To capture the influence of SMC on the coarsening process, we perform two sets of simulation: (a) two droplets, one with diameter of 60 grid cells and the other of 30 grid cells, with a distance between them of 30 grid cells, and (b) is the same as panel (a) except that the diameter of the smaller droplet is 40 grid cells. During the coarsening process, the bigger droplet grows, whereas the smaller one shrinks and tends to vanish.

To address the effect of SMC, we plot the radius of the bigger droplets increasing with time in two sets of simulation, both with and without SMC, as shown in Fig. 7. We observe that the evolution velocity of case (a) is faster than that of case (b). This is due to the fact that in case (a) the driving force, which is proportional to curvature difference of the two droplets, is higher than that of case (b). Moreover, in each case, the coarsening velocity of the two droplets is relatively unaffected, upon incorporation of Marangoni convection, although increasing the Marangoni number has a very weak enhancement of the velocity. We, therefore, conclude that SMC has no obvious effect on the mass transfer between the two droplets and thus the coarsening process is not likely to be influenced by SMC.

V. PHASE SEPARATION

A. Phase separation influenced by SMC in Fe-50 at %Sn alloy

In this section, phase separation influenced by Marangoni convection in Fe-50 at %Sn alloy is investigated. The

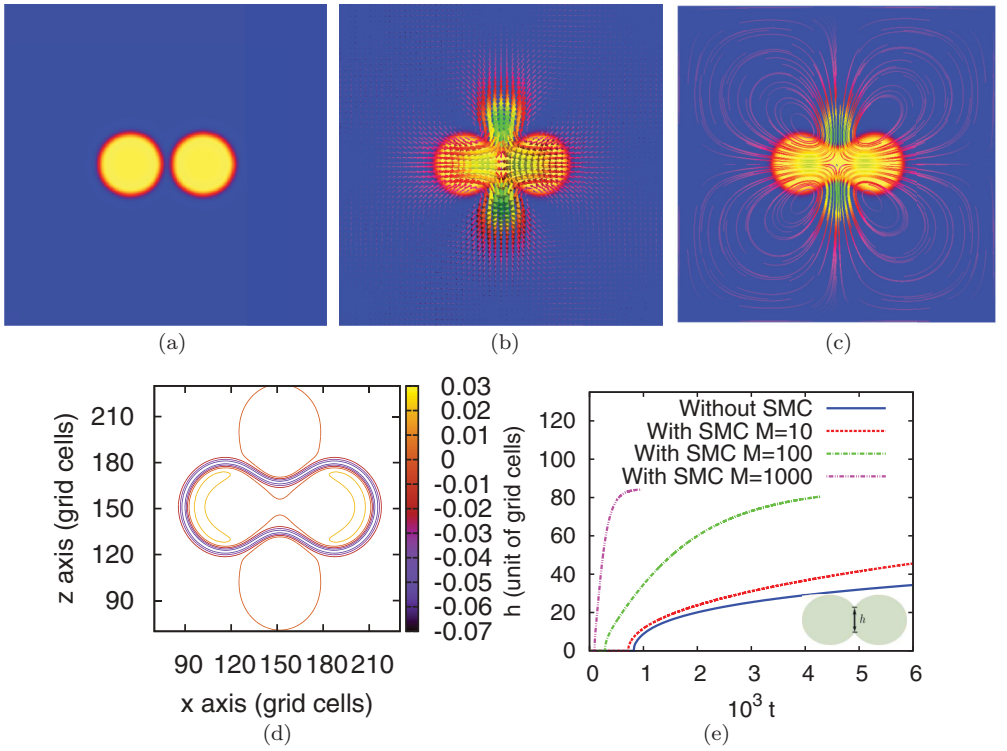

FIG. 6. (Color online) Coalescence of droplets assisted by SMC in monotectic systems: (a) is the initial morphology for simulation where two droplets are 8 grid cells distance from each other; (b) shows the coalescing morphology with the path of SMC at time of 3220; (c) illustrates the stream line that results from SMC; (d) displays the isoline of pressure caused by SMC corresponding to the state of (b); and (e) draws the height of the neck varying with time in the cases of including SMC at different Marangoni number and not considering SMC, containing the schematic figure for comprehending where we measure the height of the neck.

composition of the alloy is inside the region of the miscibility gap, where the primary liquid is unstable and in the presence of fluctuations decomposes into two liquids differing only by concentrations. Perturbation in the form of conserved noise is introduced to initiate spinodal decomposition. Based on these conditions, simulations are performed under isothermal

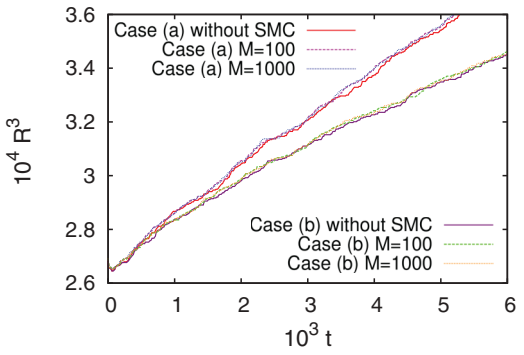

FIG. 7. (Color online) The radius of droplets as a function of time during the coarsening process: the solid red (upper) and solid brown (down) lines show cases (a) and (b) without SMC, respectively; the dashed pink (upper) and dashed green (down) lines depict cases (a) and (b) with SMC at $M = 100$, respectively; the dotted blue (upper) and dotted orange (down) lines illustrate cases (a) and (b) with SMC at $M = 1000$, respectively.

condition at a dimensionless temperature of 0.8, relating to a dimensional value of 1 122.4 K. The temperature of the spinodal decomposition at this composition of Fe-50 at %Sn is 1 781 K and the monotectic temperature of the system is 1 403 K.

At the early stage of phase separation, an incipient interface forms between the two phases and the nonuniform concentration distribution along this interface results in convection. In our simulations, the convection profile is obtained by solving the Navier-Stokes equation [Eq. (4)] with the stress tensor given by Eq. (3), including the contribution from the concentration gradient.

The concentration field together with the fluid flow profile at simulation time of 3175 is displayed in Fig. 8(b). When the concave and convex interfaces are near each other, i.e., a larger curvature difference, the convection becomes stronger. The phase separation morphology without SMC at the same time is illustrated in Fig. 8(a). A comparison between these two morphologies reveals that SMC accelerates the evolution process of phase separation in Fe-50 at %Sn alloy. Quantitative analysis is given below by making a comparison between the evolution modes in these two cases.

If an isotropic system is assumed, we can make a circular approximation to the square simulation domain and use the circular averaged concentration, which is a function of radial distance, to evaluate the spatial periodicity in the phase

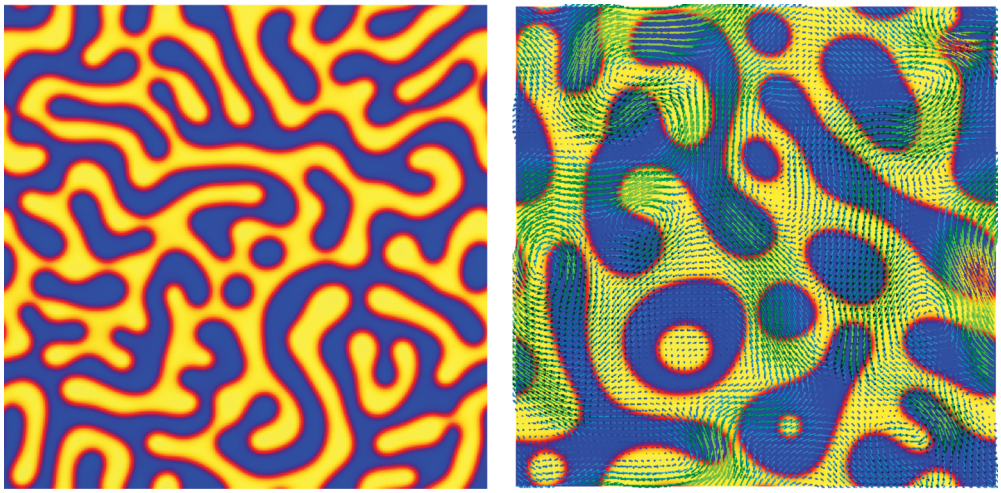

(a) (b)

FIG. 8. (Color online) Phase separation morphologies in Fe-50 at %Sn alloy without SMC (a), and with SMC (b) ($M = 10$), both at time $t = 3175$.

separation process by writing the radial distribution of the concentration as

$$C(r) = \frac{1}{N_r} \sum_{R,|R|=r} [c(r) - c_0],$$

where $c(r)$ is the concentration at each radius r, N_r is the number of the points with radius r.

In order to identify the individual modes, distinguished by the wave numbers in reciprocal space, we perform a Fourier transformation of the circular averaged concentration as

$$F(\mathbf{k}) = \int d\mathbf{r} C(r) e^{-i\mathbf{k}\cdot\mathbf{r}}. \tag{21}$$

The intensities of $F(\mathbf{k})$ with respect to the wave number at the simulation time of 425, 925, and 4 925 with and without SMC, are shown in Figs. 9(a) and 9(b), respectively. With time, the peak of $|F(\mathbf{k})|$ shifts toward the long-wave-length direction, which is in accordance with the analytical results obtained by Langer [14]. However, if we compare the peak of $|F(\mathbf{k})|$ at the same time with and without SMC, we find that the value is higher in the former case. In addition, in Fig. 9(c) we plot the amplitude of the spectra as a function of time with and without SMC, respectively. It shows that SMC dramatically accelerates the evolution process.

B. Phase separation influenced by SMC in Fe-40 at %Sn alloy

In this section, we investigate the phase separation in hypermonotectic Fe-40 at %Sn alloy influenced by SMC. Simulation conditions are the same as that in Sec. V A, initializing phase separation by using a conserved noise, which is switched off after a short evolution. The temperature of the spinodal decomposition at this composition is 1 529.9 K and the simulations are performed at a dimensionless temperature of 0.8 relating to a dimensional value of 1 122.4 K.

The morphologies resulting from spinodal decomposition at simulation time of 2 475 are shown in Figs. 10(a) and 10(b), where panel (a) refers to the case without SMC and panel (b) shows the snapshot of phase separation coupled with SMC. Compared with the bicontinuous microstructure resulted from the phase-separation of Fe-50 at %Sn alloy shown in Fig. 8, a structure composed of droplets forms at Fe-40 at %Sn alloy. Moreover, the path of fluid flow caused by the nonuniform concentration gradient is illustrated in Fig. 10(b). Notably, when two droplets begin to coalesce, the fluid flow around the contact point becomes much stronger than the other places. This is due to the fact that the negative curvature occurs at the neck of two droplets during the process of coalescence, which causes a larger difference in concentration gradient.

Figure 10(c) shows the cube of the average radius of droplets as a function of time. The solid red and dot dashed blue lines represent the cases with and without SMC, respectively, whereas the dashed green and dot dot dashed pink lines correspond to the linear fits. From the figure we conclude, without SMC the cube of average radius changes linearly with time during the evolution process, as predicted by Lifshitz and Slyozov [29] and simulation (Ref. [31]). When SMC is considered, the average radius of droplets is bigger than that not considering SMC, and the average radius as a function of time can be divided into three regimes: I (from simulation time 0 to 5 000), the average radius increases rapidly due to the fact that there is a large number of droplets with short distance between each other where SMC has a substantial accelerating effect, and this process is in accordance with the simulation obtained by Ref. [31], in which they got a $R^2 \sim t$ relation; II (from time 5 000 to 15 000), the Marangoni effect is weakened when the number of droplets decreases and the cube of the average radius of droplets changes linearly with time; III (after time 15 000), the number of droplets is fairly less, resulting in a nonsmooth increase in average radius with time. In addition, Fig. 10(d) shows the the number of droplets as a function of time for the cases with and without SMC. From the curves in Fig. 10(d), we can see that the number of droplets considering SMC is less than that without SMC. The gap between the two curves is mainly due to the initial accelerating effect of SMC

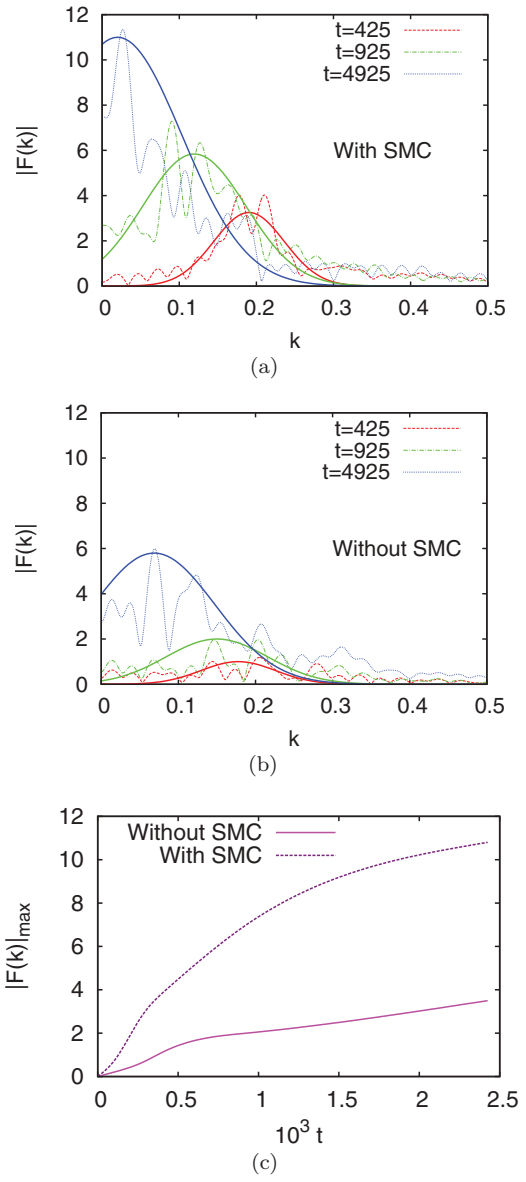

FIG. 9. (Color online) The effect of SMC on the x-ray spectra in Fe-50 at %Sn alloy: panels (a) and (b) show the intensity, calculated from Eq. (21), as a function of the wave number in the cases with and without SMC, respectively. The dashed red, dot dashed green, and dotted blue lines are for simulation time of 425, 925, and 4 925, respectively. The solid lines correspond to the fitting curves; panel (c) depicts the value of the peak of the spectra as a function of time with and without SMC, represented by the dashed purple and solid pink lines, respectively.

on the coalescence of droplets, which corresponds to regime I in Fig. 10(c).

Figures 10(e) and 10(f) present the size distribution of droplets at the simulation time of 2 475 and 9 595, respectively. In each figure, the thick solid red and thick dashed green bars represent the case without and with SMC, respectively. The short dashed pink and dot dashed cyan lines represent the Gaussian fits without and with SMC, respectively. The solid blue line is plotted to show the LSW size distribution according to Refs. [29,30] as

$$g(r) = \frac{4}{9}\left(\frac{r}{R}\right)^2 \left(\frac{3}{3+\frac{r}{R}}\right)^{7/3} \left(\frac{1.5}{1.5-\frac{r}{R}}\right)^{11/3} \exp\left(\frac{\frac{r}{R}}{\frac{r}{R}-1.5}\right),$$

where r is the radius of droplet, and R denotes the mean radius over all droplets.

Figure 10(e) shows that SMC causes a broader and flatter size distribution than that obtained without SMC, which is similar to the results obtained by Tegze *et al.* [9]. With time, the size distribution of droplets in the two cases tends to overlap each other, as shown in Fig. 10(f). A comparison with the LSW theory shows that the size distributions are broader with smaller amplitude for both cases. This is due to the fact that LSW is valid for predicting the size distribution for dilute alloys [29,30]. For high volume fraction regime, the size distribution broadens and the amplitude decreases [32–34].

Figure 11 shows the effect of SMC on the size distribution of droplets at equivalent statistical states (equal number of droplets). In the figure, we compare the size distributions at time 9 595 (without SMC) and at time 3 975 (with SMC), which are located in the linear regime in Fig. 10(c). In both cases the number of droplets is 70. It shows that the case considering SMC has a broader size distribution and the peak shifts toward the larger droplet direction. Moreover, the analytical result considering Marangoni convection, obtained by Ratke and Thieringer [37], is shown in the figure by the dashed pink line. It is observed that the size distribution of the droplets at larger and smaller size region tends to the analytical results achieved by Ratke *et al.*, whereas the LSW curve fits better around the area of $r/R = 1$.

VI. CONCLUSION

In this work we consider the Fe-Sn monotectic system and utilize the convective Cahn-Hilliard and Navier-Stokes equations for solving the equations of mass transport and phase transformation. Notably we include the capillary tensor contributed by the concentration field in the momentum balance equations and investigate the following four aspects: (a) the spontaneous motion of two droplets induced by SMC, (b) the coarsening and (c) coalescence of two droplets under the influence of SMC, and (d) the evolution modes, size distribution, mean radius, and number of droplets influenced by SMC during the phase separation process.

We find that the effect of SMC on the motion of droplets decreases dramatically with the increase in the distance between the two droplets, when the distance is beyond double the interface width. Once the interfaces of the two droplets see each other, SMC has an obvious accelerating effect on the coalescing process. Furthermore, a very weak accelerating effect of SMC is observed during the coarsening process of droplets, with increasing Marangoni number.

Moreover, we observe that SMC speeds up the phase separation process in Fe-50 %Sn and Fe-40 %Sn alloys, mainly due to the accelerating effect of SMC on coalescing process at an early stage of evolution. In addition, SMC causes a broader and flatter size distribution than that obtained without SMC and also shifts the frequency toward the larger droplet direction.

Finally, we give some remarks on the results we obtained: The Marangoni number plays a significant role during the

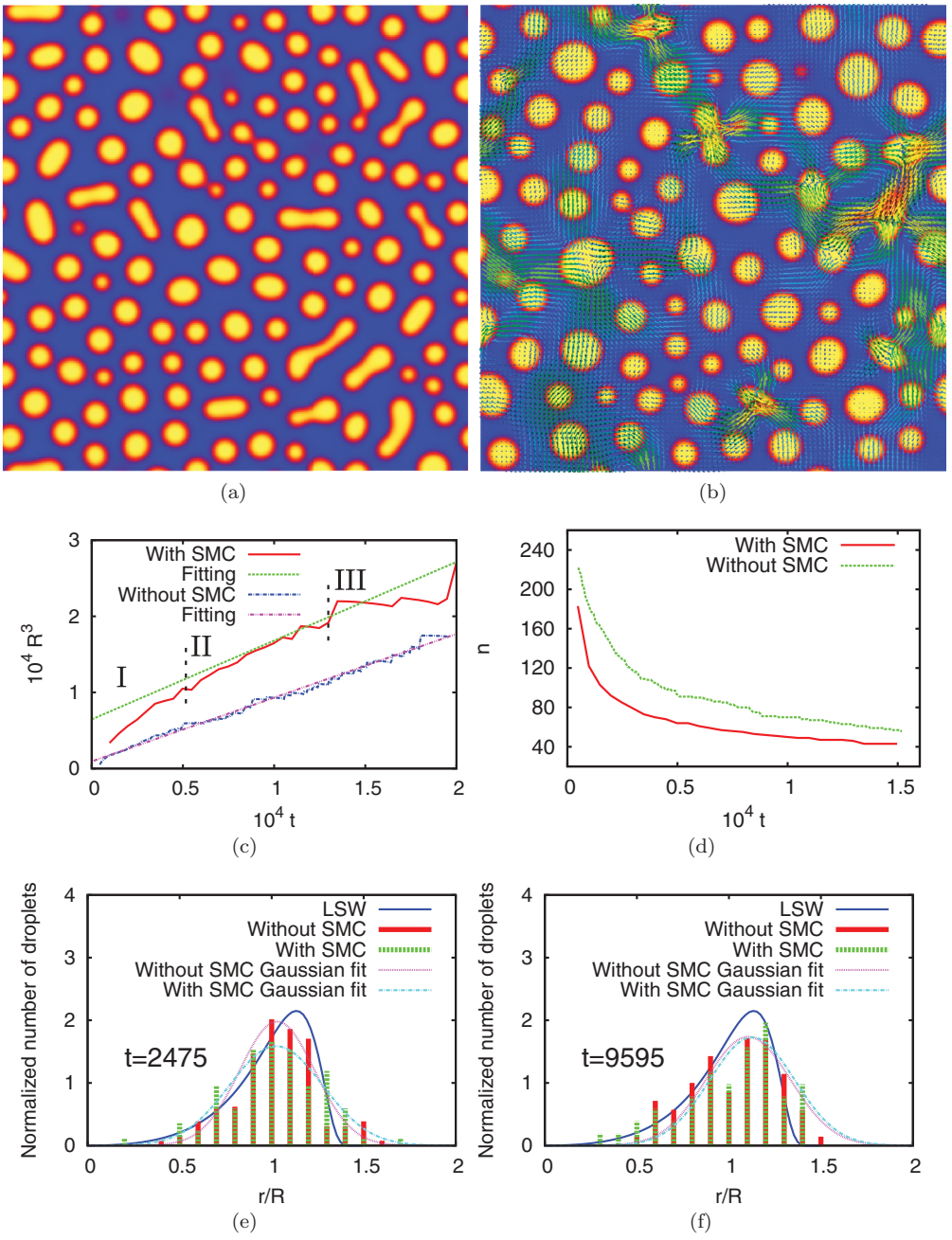

FIG. 10. (Color online) Phase separation morphologies in Fe-40 at %Sn alloy without SMC (a), and with SMC (b) ($M = 10$); the average radius and number of droplets varying with time are shown in (c) and (d), respectively. Bar chart diagrams (e) and (f) show the size distribution of droplets at simulation time of 2 475 and 9 595, respectively, in comparison with the LSW theory.

motion and coalescence process of droplets in monotectic systems. In reality, the Marangoni number is a reflection of the competition between capillary effect and bulk diffusion. Further, there exist two time scales in the problem: the one of diffusion, which is large, given that we are close to coarsening; the other is the time scale given by the ratio of the capillary forces and the viscosity of the liquid (a velocity scale and indirectly a time scale). The higher the Marangoni number, the higher the body forces are in the system, and the system is driven independently more by the convective fluid flow caused by the capillarity rather than diffusion. For smaller Marangoni numbers, diffusion plays a more dominant role, and capillary forces have a reduced effect.

ACKNOWLEDGMENTS

The authors are grateful to Q. Cheng for insightful discussions and M. Reichardt for postprocessing tool development, used in this work. F.W. thanks L. Ratke for his advice of adding RT curve for comparing. We further acknowledge financial support by the excellence center CCMSE of the state Baden-Württemberg and EFRE.

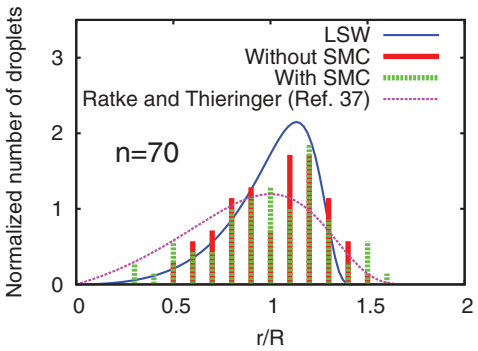

FIG. 11. (Color online) The effect of SMC on the size distribution of droplets corresponding to the equivalent statistical states.

APPENDIX A

We perform a transformation to the coordinates x and field variables $c(x)$ as

$$\xi^\mu = x^\mu + w^\mu_\nu x^\nu + a^\mu \equiv x^\mu + \kappa^\mu(x), \tag{A1}$$

$$\phi(\xi) = c(x) + \delta c(x), \tag{A2}$$

where a^μ represents a space time translation, and w^μ_ν is a Lorenz transformation and antisymmetry. ξ is the new coordinate and $\phi(\xi)$ is the new field variable after transformation.

According to Noether's theorem [35], a specific transformation of the coordinates and field variables does not change the action

$$\delta S = \int_{\Omega'} \mathcal{L}[\phi(\xi), \partial'_\mu \phi(\xi)] d\Omega' - \int_\Omega \mathcal{L}[c(x), \partial_\mu c(x)] d\Omega = 0. \tag{A3}$$

For a scalar field $\phi(\xi) = c(x)$ and using $d\Omega' = d\Omega$, we write

$$\int_{\Omega'} \mathcal{L}[\phi(\xi), \phi'_{,\mu}(\xi)] d\Omega' = \int_\Omega \mathcal{L}[c(x), \partial'_\mu c(x)] d\Omega. \tag{A4}$$

Combining with Eq. (A1), we obtain

$$\partial'_\mu = \frac{\partial x^\nu}{\partial \xi^\mu} \partial_\nu = \partial_\mu - (\partial_\mu \kappa^\nu)\partial_\nu.$$

Substituting the above expression in Eq. (A4) and expanding it, we get

$$\int_\Omega \mathcal{L}\{c, [\partial_\mu - (\partial_\mu \kappa^\nu)\partial_\nu]c\} d\Omega = \int_\Omega \mathcal{L}(c, \partial_\mu c) d\Omega - \int_\Omega \frac{\partial \mathcal{L}}{\partial(\partial_\mu c)} (\partial_\mu \kappa^\nu)\partial_\nu c d\Omega. \tag{A5}$$

The second term in Eq. (A5) can be written as

$$\frac{\partial \mathcal{L}}{\partial(\partial_\mu c)} (\partial_\mu \kappa^\nu)\partial_\nu c = \partial_\mu \left[\frac{\partial \mathcal{L}}{\partial(\partial_\mu c)} \kappa^\nu \partial_\nu c \right] - \kappa^\nu \partial_\mu \left[\frac{\partial \mathcal{L}}{\partial(\partial_\mu c)} \partial_\nu c \right]. \tag{A6}$$

Using the Euler-Lagrange equation $\frac{\partial \mathcal{L}}{\partial c} = \partial_\mu \frac{\partial \mathcal{L}}{\partial(\partial_\mu c)}$, the last term can be rewritten as

$$\partial_\nu \mathcal{L} = \partial_\mu \left[\frac{\partial \mathcal{L}}{\partial(\partial_\mu c)} \partial_\nu c \right].$$

Thus, when we use $\partial_\nu \kappa^\nu = 0$ due to the antisymmetry of $w_{\mu\nu}$, Eq. (A3) reads as

$$\delta S = -\int_\Omega \partial_\mu \left[\frac{\partial \mathcal{L}}{\partial(\partial_\mu c)} \kappa^\nu \partial_\nu c - \kappa^\mu \mathcal{L} \right] d\Omega.$$

Since the action is assumed to be invariant under the transformation in Eqs. (A1) and (A2) for arbitrary volumes Ω, we have a conserved current, $\partial_\mu \Theta^\mu = 0$, with

$$\Theta^\mu = \frac{\partial \mathcal{L}}{\partial(\partial_\mu c)} \kappa^\nu \partial_\nu c - \kappa^\mu \mathcal{L}.$$

By writing

$$\Theta^\mu_\nu = \frac{\partial \mathcal{L}}{\partial(\partial_\mu c)} \partial_\nu c - \delta^\mu_\nu \mathcal{L},$$

our conservation law $\partial_\mu \Theta^\mu = 0$ now implies

$$\partial_\mu \Theta^\mu_\nu = 0.$$

APPENDIX B

The coefficients in Eq. (13), which are used to achieve the concentration profile in Sec. III A, are written as,

$$g^n_{-1} = n \sin h\left[\left(n - \tfrac{1}{2}\right)a\right],$$

$$g^n_0 = (1 + 2\varsigma)\chi \cosh\left[\left(n + \tfrac{1}{2}\right)a\right] + (2n + 1)\cosh a \sinh\left[\left(n + \tfrac{1}{2}\right)a\right],$$

$$g^n_1 = (n + 1)\sinh\left[\left(n + \tfrac{3}{2}\right)a\right].$$

The matrices, $\mathbf{t}_n$, $\mathbf{v}_n$, and Ξ_n in Eq. (16), which are used to calculate the stream function and the moving velocity of droplets, are listed below:

$$\mathbf{t}_n = \left[0,0,0,0,0,0,E^{(a)}_n, -E^{(-a)}_n\right]^T$$

$$\mathbf{v}_n = \left[F^{(a)}_n, F^{(-a)}_n, F^{(a)}_n, F^{(-a)}_n, 0,0,0,0\right]^T,$$

with

$$E_n^{(\pm a)} = n(n+1)\left\{\frac{\pm 1}{2\chi(1+2\varsigma)}\left[-4\sqrt{2}e^{-(n+\frac{1}{2})a} \pm G_{n-1}\sinh\left(n-\frac{1}{2}\right)a \mp G_{n+1}\sinh\left(n+\frac{3}{2}\right)a\right] + G_n\cosh\left(n+\frac{1}{2}\right)a\right\}$$

$$F_n^{(\pm a)} = \frac{1}{2\sqrt{2}}n(n+1)\left[\frac{e^{-(n-\frac{1}{2})a}}{n-\frac{1}{2}} - \frac{e^{-(n+\frac{3}{2})a}}{n+\frac{3}{2}}\right]$$

$$\Xi_n = \begin{pmatrix} 0 & 0 & 0 & 0 & e^{(-a)} & e^{(a)} & 0 & 0 \\ 0 & 0 & 0 & 0 & 0 & 0 & e^{(-a)} & e^{(a)} \\ c^{(-a)} & s^{(-a)} & c^{(a)} & s^{(a)} & 0 & 0 & 0 & 0 \\ c^{(-a)} & -s^{(-a)} & c^{(a)} & -s^{(a)} & 0 & 0 & 0 & 0 \\ n_- s^{(-a)} & n_- c^{(a)} & n_+ s^{(a)} & n_+ c^{(a)} & n_- e^{(-a)} & n_+ e^{(a)} & 0 & 0 \\ -n_- s^{(-a)} & n_- c^{(-a)} & -n_+ s^{(a)} & n_+ c^{(a)} & 0 & 0 & -n_- e^{(-a)} & -n_+ e^{(a)} \\ n_-^2 c^{(-a)} & n_-^2 s^{(-a)} & n_+^2 c^{(a)} & n_+^2 s^{(a)} & -n_-^2 e^{(-a)} & -n_+^2 e^{(a)} & 0 & 0 \\ n_-^2 c^{(-a)} & -n_-^2 s^{(-a)} & n_+^2 c^{(a)} & -n_+^2 s^{(a)} & 0 & 0 & -n_-^2 e^{(-a)} & -n_+^2 e^{(a)} \end{pmatrix}$$

with $n_- = n - \frac{1}{2}$, $n_+ = n + \frac{3}{2}$, $c^{(\pm a)} = \cosh n_\pm a$, $s^{(\pm a)} = \sinh n_\pm a$, $e^{(\pm a)} = e^{-n_\pm a}$.

APPENDIX C

Equation (15) can be written as

$$u_\iota = U\mathbf{i}_z \cdot \mathbf{i}_\iota, \tag{C1}$$

with

$$\mathbf{i}_z \cdot \mathbf{i}_\iota = -(\cosh\iota - \cosh\varphi)\frac{\partial x}{\partial \varphi}.$$

With the aid of Eq. (14), Eq. (C1) can be expressed as

$$\frac{\partial}{\partial\varphi}\left(\psi + \frac{1}{2}Ux^2\right) = 0. \tag{C2}$$

Integrating over the surface of droplets, we thus obtain Eq. (15).

[1] C. Stöcker and L. Ratke, J. Crystal Growth **203**, 582 (1999).
[2] C. Stöcker and L. Ratke, J. Crystal Growth **212**, 324 (2000).
[3] B. Nestler, A. A. Wheeler, L. Ratke, and C. Stöcker, Physica D **141**, 133 (2000).
[4] L. Ratke, Metall. Mater. Trans. A **34**, 449 (2003).
[5] R. Borcia and M. Bestehorn, Phys. Rev. E **67**, 066307 (2003).
[6] K. Nagai, Y. Sumino, H. Kitahata, and K. Yoshikawa, Phys. Rev. E **71**, 065301 (2005).
[7] X. Fanton and A. M. Cazabat, Langmuir **14**, 2554 (1998).
[8] J. Zhang, R. P. Behringer, and A. Oron, Phys. Rev. E **76**, 016306 (2007).
[9] G. Tegze, T. Pusztai, and L. Gránásy, Mater. Sci. Eng. A **413-414**, 418 (2005).
[10] V. E. Badalassi, H. D. Ceniceros, and S. Banerjee, J. Comput. Phys. **190**, 371 (2003).
[11] J. Kim, Commun. Comput. Phys. **12**, 613 (2012).
[12] U. Thiele, K. John, and M. Bär, Phys. Rev. Lett. **93**, 027802 (2004).
[13] J. W. Cahn, J. Chem. Phys. **42**, 93 (1965).
[14] J. S. Langer, Acta Metall. **21**, 1649 (1973).
[15] L. Ratke, G. Korekt, and S. Drees, Adv. Space Res. **22**, 1227 (1998).
[16] A. A. Golovin, A. Nir, and L. M. Pismen, Ind. Eng. Chem. Res. **34**, 3278 (1995).
[17] R. Monti, R. Savino, and G. Alterio, Acta Astronaut. **51**, 789 (2002).
[18] I. Egry, D. Herlach, M. Kolbe, L. Ratke, S. Reutzel, C. Perrin, and D. Chatain, Adv. Eng. Mater. **5**, 819 (2003).
[19] J. W. Cahn and J. E. Hilliard, J. Chem. Phys. **28**, 258 (1958).
[20] G. Muñoz, Am. J. Phys. **64**, 1153 (1996).
[21] D. M. Anderson, G. B. McFadden, and A. A. Wheeler, Annu. Rev. Fluid Mech. **30**, 139 (1998).
[22] D. M. Anderson, G. B. McFadden, and A. A. Wheeler, Physica D **135**, 175 (2000).
[23] J. J. Hoyt, M. Asta, and B. Sadigh, Phys. Rev. Lett. **85**, 594 (2000).

[24] M. Grieble, T. Dornseifer, and T. Neunhoeffer, *Numerical Simulation in Fluid Dynamics: A Practical Introduction* (The Society for Industrial and Applied Mathematics, Philadelphia, 1997).
[25] M. Meyyappan, W. R. Wilcox, and R. S. Subramanian, J. Colloids Interface Sci. **94**, 243 (1983).
[26] L. M. Witkowski and J. S. Walker, Phys. Fluids **14**, 2647 (2002).
[27] M. Stimson and G. B. Jeffery, Proc. R. Soc. A **111**, 110 (1926).
[28] A. A. Golovin and L. M. Pismen, Chaos **14**, 845 (2004).
[29] I. M. Liftshitz and V. V. Slyozov, J. Phys. Chem. Solids **19**, 35 (1961).
[30] C. Wagner, Z. Elektrochem **65**, 581 (1961).
[31] H.-J. Diepers, C. Beckermann, and I. Steinbach, Acta Mater. **47**, 3663 (1999).
[32] S. P. Marsh and M. E. Glicksman, Acta Mater. **44**, 3761 (1996).
[33] W. Bender and L. Ratke, Acta Mater. **46**, 1125 (1998).
[34] D. J. Rowenhorst, J. P. Kuang, K. Thornton, and P. W. Voorhees, Acta Mater. **54**, 2027 (2006).
[35] E. Noether and M. A. Tavel, Transp. Theory Statist. Phys. **1**, 186 (1971).
[36] A. E. Rednikov and Yu. S. Ryazantsev, Fluid Dynam. **25**, 753 (1990).
[37] L. Ratke and W. K. Thieringer, Acta Metall. **33**, 1793 (1985).